# Observation of intermediate mixed state in high-purity cavity-grade Nb by magneto-optical imaging

S. Ooi,[1] M. Tachiki,[1] T. Konomi,[2,3] T. Kubo,[2,3] A. Kikuchi,[4] S. Arisawa,[4] H. Ito,[2] and K. Umemori[2,3]

[1]*International Center for Materials Nanoarchitectonics, National Institute for Materials Science, Sengen 1-2-1, Tsukuba 305-0047, Japan*

[2]*High Energy Accelerator Research Organization, 1-1 Oho, Tsukuba 305-0801, Japan*

[3]*SOKENDAI (The Graduate University for Advanced Studies), Hayama 240-0193, Japan*

[4]*Research Center for Functional Materials, National Institute for Materials Science, Sengen 1-2-1, Tsukuba 305-0047, Japan*

(Received 20 April 2021; revised 6 July 2021; accepted 13 July 2021; published 9 August 2021)

Suppression of the occurrence of remanent vortices is necessary to improve the quality factor of superconducting resonators. In particular, the flux-expulsion dynamics in Nb during cooling has become of major interest to researchers focusing on superconducting cavities. To study the vortex states and their behavior in high-purity cavity-grade Nb, we used a magneto-optical imaging technique to perform real-space observations of the magnetic field distributions during the field-cooling and field-scanning processes. In the field-cooling process, the distributions were observed to undergo phase separation into vortex and Meissner regions, as would be expected in an intermediate mixed state (IMS). The vortex regions in the IMS, such as vortex bundles, tend to be larger in higher fields, in contrast to the Meissner regions, which experience shrinkage. In the field-scanning process, domelike field profiles, which indicate a geometrical barrier with very weak bulk pinning, were observed. The existence of the IMS suggests that cavity-grade Nb is in a type-II/1 superconductor regime, in which attractive interaction between vortices at a length scale of the penetration depth is crucial for the behavior of vortices.

DOI: 10.1103/PhysRevB.104.064504

## I. INTRODUCTION

Superconducting resonators are essential components of cutting-edge superconducting devices, including quantum information technologies [1], kinetic inductance detectors (KIDs) for cosmological and astronomical observations [2], and superconducting radio-frequency (SRF) cavities for particle accelerators [3]. The quality factors ($Q$) of these devices have been improved by optimizing the resonator geometry [3–6], improving the materials processing and fabrication technologies [7–10], and by conducting theoretical studies based on the microscopic theory of superconductivity [11–15]. Among these, Nb SRF technology allows us to achieve the highest $Q$ factor, which routinely reaches $Q \sim 10^{11}$. One of the lessons learned in the last few decades is the importance of reducing the occurrence of remnant vortices that have not been expelled from resonator materials. They cause the $Q$ factor to deteriorate because of the dissipation of energy in the oscillating normal core of the vortices [16,17]. Therefore, improving the $Q$ factor would necessitate the perfect expulsion of these vortices during cool down in the weak magnetic field that remains even after elaboration to remove the field by using magnetic shields or implementing active cancellation [4,18]. Understanding the behavior of vortices in high purity cavity-grade Nb is expected to be profitable to refine several reported methods to realize the perfect flux expulsion [19–21].

Niobium, a well-known type-II superconductor with the highest $T_c$ among the single element materials, has been extensively studied. However, the magnetic phase diagram in the superconducting state of high-purity Nb is somewhat peculiar, because the Ginzburg-Landau (GL) parameter $\kappa$ is very close to the critical value of $1/\sqrt{2}$, which separates type-I and type-II superconductors [22,23]. In low $\kappa$ type-II superconductors like the high-purity Nb, an additional vortex state, known as the intermediate mixed state (IMS), has been experimentally and theoretically confirmed to exist between the Meissner and mixed (vortex) states. These superconductors are referred to as "type-II/1" superconductors [23]. Many decades ago, the spatial coexistence of the Meissner and vortex regions, in the form of, e.g., vortex bundles (or vortex islands) embedded in the Meissner state, were visualized in the IMS by the Bitter decoration technique [24,25]. The existence of a potential minimum in vortex-vortex interaction at the length scale of the penetration depth $\lambda$ is a possible origin of the aggregation of vortices in the IMS [23]. More recently, the IMS has provoked new interest in attractive vortex-vortex interactions and the state was reexamined by using several advanced experimental techniques, e.g., small angle neutron diffraction for Nb [26–28] or scanning Hall probe microscopy for $ZrB_{12}$ [29,30]. Theoretically, the vortex phase diagram of superconductors with $\kappa$ close to $1/\sqrt{2}$ is still a fascinating subject that continues to stimulate new theoretical studies [31,32].

Regarding the improvement of the $Q$ factor of SRF cavities, it is important to investigate whether the IMS exists in cavity-grade Nb, because the formation of vortex bundles is expected to be closely related to the expulsion of vortices if they exist. For this purpose, magneto-optical (MO) imaging is a convenient and powerful technique to visualize the magnetic field distributions of superconductors in real space and

 

time [33]. Recently, Koeszegi *et al.* studied the influence of a twin boundary and precipitations of niobium hydride $NbH_x$ on vortex pinning in Nb by the MO imaging technique [34]. However, vortex structures such as bundles or chains, which is expected in the IMS, were not identified. In this paper we present the MO observation of phase separations in the IMS during a temperature scan ($T$ scan, or field cooling) at constant magnetic fields and a field scan ($H$ scan) at constant temperatures for single crystalline cavity-grade Nb.

## II. EXPERIMENTS

Single-crystalline Nb samples of a cuboid shape ($7.2\times7.2\times3.0$ mm$^3$) were cut out from a wide Nb plate, with a thickness of 3 mm, containing a few large grains (Tokyo Denkai Co.). This is one of plates in the same lot which were used to fabricate SRF cavities. The residual-resistance ratio (RRR) of the pristine plate is 496 from the material's specification sheet. The samples were annealed at 900 °C under high vacuum ($\sim10^{-4}$ Pa) for 3 h to sufficiently remove absorbed hydrogen gas after the preparation of mirror surfaces by mechanical and chemical polishing. According to the theoretical relation between RRR and the GL parameter $\kappa$ (Appendix A), the value of $\kappa$ of our Nb samples is expected to be in the range 0.73–0.81 based on the reported value of $\kappa_0$ for ideal pure Nb ($\kappa_0$: 0.713 [35], 0.78 [22], or 0.79 [36]).

Our experimental setup, which is schematically shown in Fig. 1(a), is a typical setup for low-temperature MO observations. The equipment consists of a polarizing microscope with a polarizer and analyzer arranged in a crossed-Nicol configuration, a liquid-He-flow cryostat, and a coil to apply a magnetic field $H_a$. The MO indicators, a key component of MO imaging intended to convert the strength of magnetic induction $B$ to light intensity $I$, are commercially available garnet-based sensors with mirror and protection layers (Matesy GmbH). Images were captured using a cooled CCD camera (Retiga EXi fast 1394, QImaging) in a $T$-scan or $H$-scan process, as illustrated in Fig. 1(b). The sequential images corresponding to Figs. 4 and 5 are provided as movies in the Supplemental Material [37].

In our setup, $I(x,y)$ is approximately expressed as $[a_0(x,y)B(x,y)+b_0(x,y)]^2+I_0$, where the constants $a_0$ and $b_0$ have a position dependence which mainly originates from the polarizing microscope itself. Magnetic induction images ($B$ images) were calculated from the source image via the following simple conversion procedure:

(1) Subtract a constant background value $I_0$ from the entire view, then take the square root thereof, $\sqrt{I(x,y,H,T)-I_0}$.

(2) From the result of (1), subtract a zero-field image taken at a temperature $T_0$ above $T_c$, $\sqrt{I(x,y,H,T)-I_0}-\sqrt{I(x,y,0,T_0)-I_0}$.

(3) Normalize the results of (2) by an image taken in a field $H_0$ at $T_0$, $\frac{\sqrt{I(x,y,H,T)-I_0}-\sqrt{I(x,y,0,T_0)-I_0}}{\sqrt{I(x,y,H_0,T_0)-I_0}-\sqrt{I(x,y,0,T_0)-I_0}}H_0$.

An application example of this conversion is shown in the Supplemental Material [37]. In $B$ images, the position-dependent $a$ and $b$ of the source images can be normalized. Inevitable errors occur occasionally due to the abrupt motions of zigzag magnetic domain walls of the garnet MO sensor during changes in the field or temperature, because a change in the in-plane component of the field at the sensor influences positions of the domain walls [38]. However, these errors are usually noticeable in images.

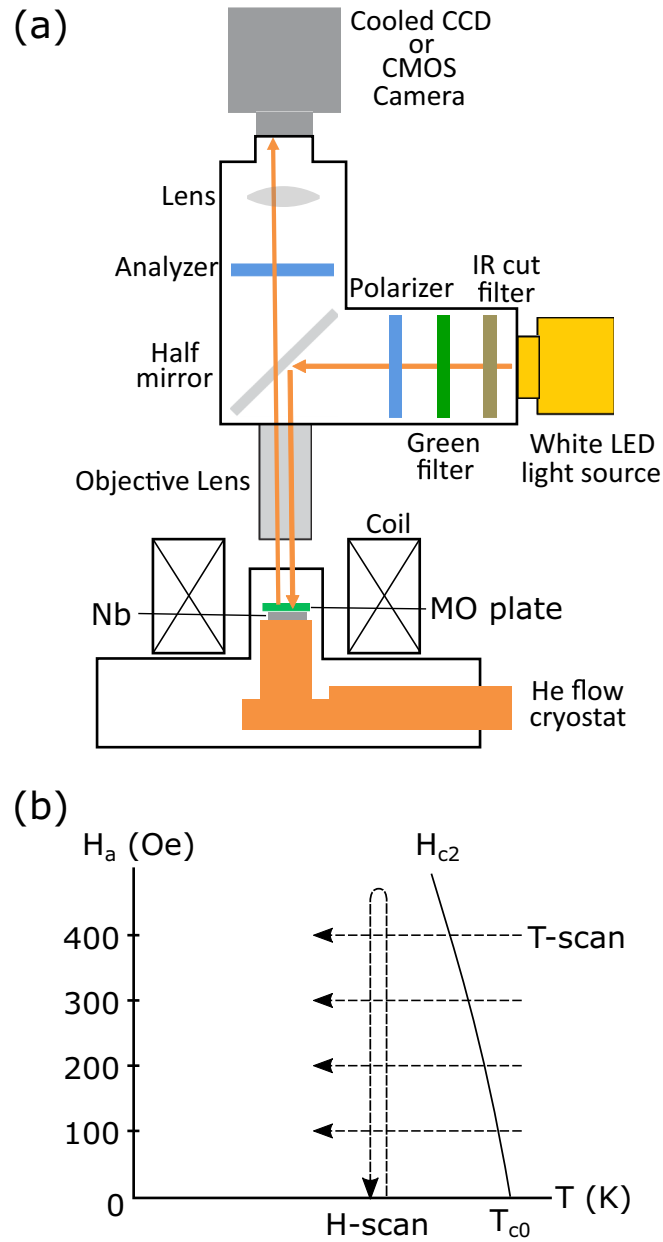


FIG. 1. (a) Schematic illustration of the MO imaging setup. Incident polarized light passing through a polarizer, green, and IR-cut filters from a white LED light source, is reflected at the mirror layer of the MO indicator. In the sensor layer of the indicator, the polarization angle rotates linearly depending on the magnitude of the vertical component of the local magnetic field $B$ at the position. In the crossed-Nicol configuration, therefore, a captured image reflects the distribution of $B$. Ideally, the intensity of the reflected light is proportional to $B^2$ after passing through the analyzer. (b) Our experimental processes of the $T$ scan and $H$ scan on the $H_a$-$T$ plane.

## III. RESULTS AND DISCUSSIONS

MO images captured at 5.9 K after field cooling in 100 Oe are shown in Fig. 2. We successfully observed phase

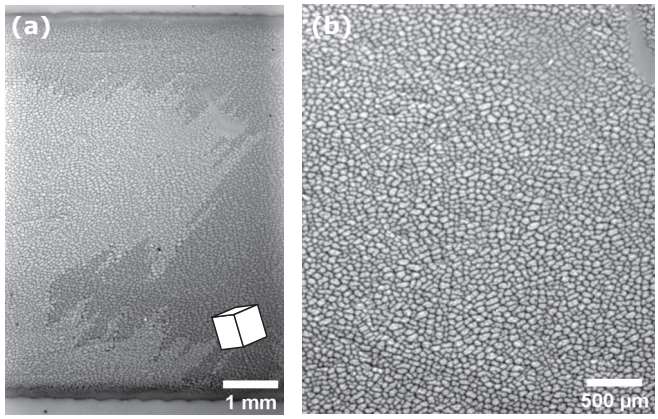


FIG. 2. (a) MO image of the IMS on the mirror-polished surface of the Nb crystal at $5.9 \pm 0.05$ K after field cooling in 100 Oe. The two regions with different contrasts separated by zigzag lines are caused by the magnetic domains of the MO sensor. The crystallographic orientation of the Nb sample is indicated by a drawing of the unit cell. (b) MO image of the IMS at the center of the sample in a different experimental run with the same condition of the temperature and field as (a).

separation into vortex (bright) and Meissner (dark) regions, indicating the existence of the IMS. To the best of our knowledge, this is the first MO visualization of the IMS in cavity-grade Nb. The observed patterns of the IMS are rather similar to that of the Meissner and normal domains in the intermediate state of the type-I superconductor Pb reported by Prozorov *et al.* [39,40]. They treated the normal domains as a kind of froth, called as "suprafroth," and analyzed the structures topologically [40]. In our observations it seems that the crystallographic axes and edges are not related to the patterns of IMS in Nb. Additionally, the patterns change every time in different cooling cycles (see the Supplemental Material [37]).

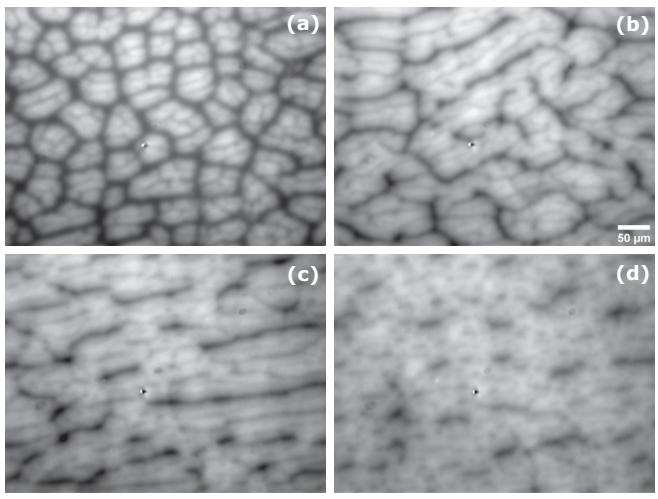


FIG. 3. MO images of the IMS at higher magnification at ∼5.9 K after field cooling in (a) 100 Oe, (b) 200 Oe, (c) 300 Oe, and (d) 400 Oe. All images are captured at the same position, which is not close to the sample edges. The orientation of the sample is the same as that in Fig. 2.

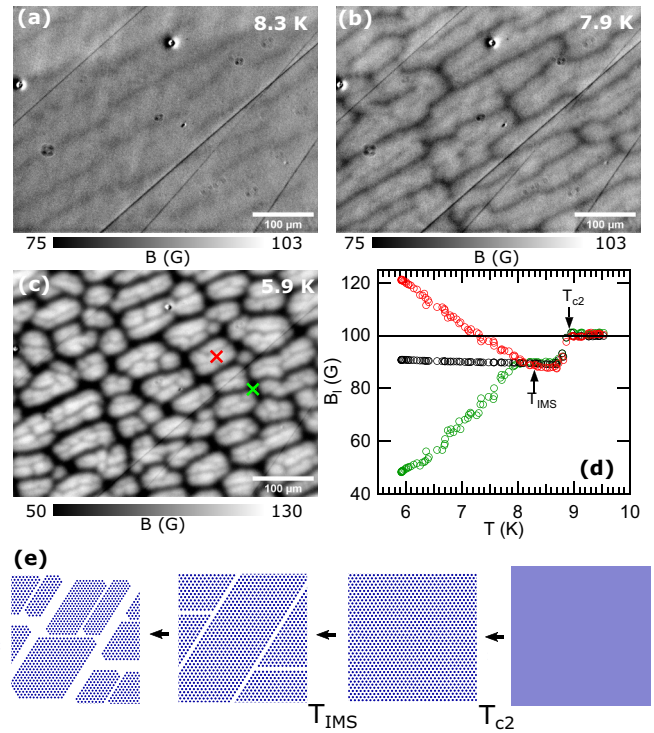


FIG. 4. (a)–(c) Magnetic induction images at 8.3, 7.9, and 5.9 K, respectively, captured in 100 Oe in the $T$-scan process [see Fig. 1(b)] at a position not close to the edges. (d) Temperature dependence of local magnetic induction $B_l(T)$ in a vortex bundle (red) and Meissner phase (green), the sampling positions of which are indicated in (c). The black circles show the averaged value of $B$ in each entire image. (e) Schematic illustration of phase separation from $T > T_{c2}$ (right) to lower temperatures (left).

Figure 3 shows MO images at a higher magnification at 5.9 K after field cooling in various magnetic fields at a position not close to the sample edges. The vortex bundles surrounded by the Meissner state are clearly observed in Fig. 3(a). Their lateral sizes are 50 to 100 $\mu$m and the shapes are approximately irregular polygons in a magnetic field of 100 Oe. Interestingly, several fine cracks can be observed to exist within each bundle. Although the origin of the fine cracks is unclear, they may emerge near the surface only and not exist at the inside of samples because of the change of magnetic field distribution across the surface. At 200 Oe, the domains of the vortex state tend to be larger, and show an intricate pattern as shown in Fig. 3(b). In higher fields, Figs. 3(c) and 3(d), the Meissner regions appear to be linear in shape or exist in the form of tiny cracks in a large plane of the vortex state, while the total area of the Meissner regions shrinks as the field increases.

To observe the way in which phase separation into the vortex and Meissner domains occurs during the field-cooling process, a series of MO images was captured by decreasing the temperature in steps of 0.05 K ($T$ scan). The $B$ images calculated for 100 Oe are shown in Figs. 4(a)–4(c). Soon after the superconducting transition at ∼8.9 K, the diamagnetic response of Nb lowers $B$ by approximately 10% uniformly. The superconducting transition temperature in magnetic fields $T_{c2}(H)$ is determined at the onset of the decrease in $B(T)$. As

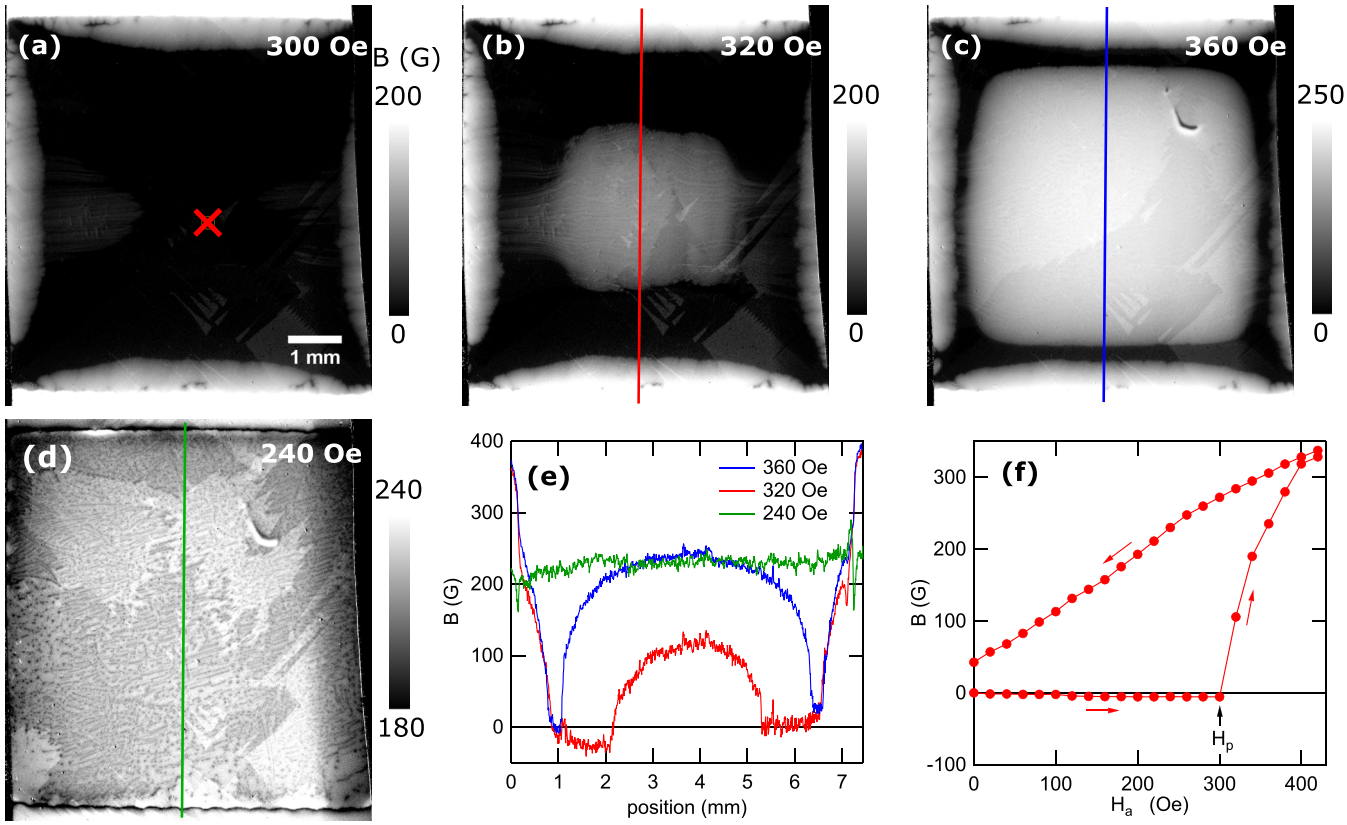


FIG. 5. (a)–(d) $B$ images in 300, 320, 360, and 240 Oe, respectively, with increasing field up to 420 Oe and then decreasing field at 7.5 K [$H$-scan process in Fig. 1(b)]. (e) Profiles on the red, blue, and green lines in (b)–(d), respectively, where the origin of the horizontal axis corresponds to the upper edge of the line. Domelike field profiles are observed at the center of the sample in (b) and (c). (f) Local magnetic induction $B_{\mathrm{l}}$ at the position marked by a red cross in (a), with increasing and decreasing applied field $H_{\mathrm{a}}$. The field where vortices start to rapidly penetrate the center is defined as the penetration field $H_{\mathrm{p}}$.

shown in Fig. 4(a), a lamellarlike structure, consisting of elongated vortex domains and unidirectional linear cracks of the Meissner phase, suddenly appears below a certain temperature 8.3 K for 100 Oe, which we define as the transition temperature to the IMS $T_{\mathrm{IMS}}(H)$. As the temperature is decreased further, the vortex domains are increasingly fractionated by newly emerged cracks and appear more well defined, as shown in Figs. 4(b) and 4(c). The observed evolution of the phase separation during cool down is schematically illustrated in Fig. 4(e).

The temperature dependence of the local magnetic induction $B_{\mathrm{l}}$ at positions inside and outside of the vortex domains are plotted in Fig. 4(d) with the averaged $B$ of the entire view. The averaged $B$ is almost constant below $T_{\mathrm{c}}$, whereas $B_{\mathrm{l}}$ in the vortex domain starts to increase below $T_{\mathrm{IMS}}$, indicating that the vortices in the vortex domain become denser with decreasing temperature. Outside the vortex domain, $B_{\mathrm{l}}$ decreases. Although $B_{\mathrm{l}}$ should be ideally zero in the Meissner state, finite values of $B_{\mathrm{l}}$ are detected because of the spread of the magnetic field from the vortex domains into the gap between the MO sensor layer and the surface of Nb.

Figure 5 shows the behavior of vortex penetration or exit during up and subsequent down scanning of the field at 7.5 K following zero-field cooling ($H$ scan). Although the screening current prevents the magnetic field from entering the sample below 300 Oe, except near the edges [Fig. 5(a)], the magnetic field starts to penetrate the center of the sample above 320 Oe, as shown in Fig. 5(b). Interestingly, streamlines of the vortex flow are observed to penetrate the sample from the right and left edges, because of the visibility of the vortex bundles, which appear in $B_{\mathrm{l}} <\sim 250$ G at this temperature. The vortices accumulated around the center exhibit domelike field distribution, the profile of which is shown in Fig. 5(e). This is because of the so-called geometrical barrier which is expected in samples with angular corners in the cross section parallel to the magnetic field [41,42]. Further increases in the applied field cause additional vortices to accumulate at the center, whereupon the dome profile grows larger and wider [Figs. 5(c) and 5(e)]. In Fig. 5(c) it is still possible to see the IMS with bright and dark regions across the entire dome.

As the magnetic field is swept down after reaching 420 Oe, the dome profile gradually collapses and almost becomes flat below 260 Oe. As shown in Fig. 5(d), many Meissner cracks are generated at 240 Oe, indicating the appearance of the IMS. The hysteretic behavior of $B_{\mathrm{l}}$ in the central region of the sample is shown in Fig. 5(f) with the definition of the penetration field $H_{\mathrm{p}}$, in which the vortices start to penetrate. The observed dome and flat field profiles in the increasing and returning $H$ scans, respectively, suggest that the pinning effect in this Nb sample is quite weak [41].

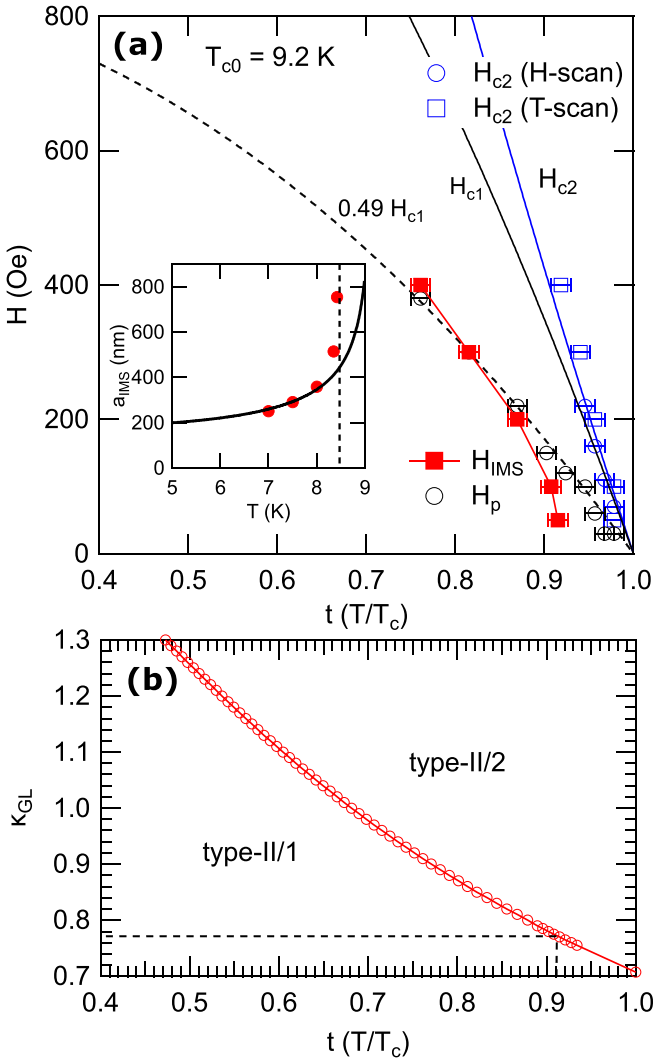


FIG. 6. (a) Experimentally obtained temperature dependence of $H_{IMS}$ (red squares), which is the upper boundary of the IMS, the penetration field of vortices $H_p$ (black circles), and $H_{c2}$ (blue circles and squares) in the single-crystal niobium. The black and blue solid lines indicate the temperature dependence of $H_{c1}$ and $H_{c2}$ obtained by Finnemore *et al.* [22]. The dashed line is $H_{c1}$ scaled by a factor of 0.49, to fit to $H_p$. The inset shows the temperature dependence of the lattice constant of the vortex lattice at the upper boundary of the IMS, which is converted from $B_{IMS}(T)$. (b) Theoretical phase boundary between type II/2 (normal type II) and type II/1 in the $\kappa$-$T$ phase diagram.

The phase boundaries were studied by extracting the values of $T_{IMS}(H)$, $H_p(T)$, and $H_{c2}(T)$ from the $T$-scan and $H$-scan MO observations. Here $H_{c2}(T)$ by $T$ scan is the same data as $T_{c2}(H)$, whose definition is illustrated in Fig. 4, and $H_{c2}(T)$ by $H$ scan is determined as a field where the field profile across the edges becomes flat, which indicates the diamagnetic response disappears. These results are summarized in Fig. 6, together with the $H_{c1}$ and $H_{c2}$ lines of reference obtained by Finnemore *et al.*, in which long-shaped Nb samples were used to eliminate the demagnetization effect [22]. While our value of $H_{c2}(T)$ almost coincides with the line of reference, $H_p$ is almost half of $H_{c1}$ of the reference. In our cuboid samples, $H_p$ is lower than the true $H_{c1}$ owing to the demagnetization effect. According to the model of the geometrical barrier [41–43], the suppression of $H_p$ can be estimated by $H_p \sim (2H_{c1}/\pi)\sqrt{d/w}$, where $d$ and $w$ are the thickness and half-width of a sample with a rectangular cross section. Although the model assumed a thin strip-shaped sample ($d \ll w$), the estimation $H_p \sim 0.58H_{c1}$ is not far from the observed value of 0.49.

$H_{IMS}(T)$ has a temperature dependence similar to that of $H_p$ ($\propto H_{c1}$) except a deviation in the vicinity of $T_c$. Note that the coincidence of the absolute values of $H_{IMS}(T)$ and $H_p$ is not intrinsic, because $H_p$ is significantly influenced by the shape of the samples, as mentioned above. It seems that $T_{IMS}$ is restricted below 8.4 K($t_{IMS}^{max} \sim 0.91$) at lower fields, which may be related to the transition from normal type II (type II/2) to type II/1 with decreasing temperature [35,44,45]. Figure 6(b) shows the phase boundary of these phases in the $\kappa$-$t$ phase diagram, which is numerically calculated using Kramer's asymptotic theory [44], as explained in Appendix B. In Fig. 6(b), $t \sim 0.91$ corresponds to $\kappa \sim 0.77$, which is in the expected range for our Nb samples.

The temperature dependence of $H_{IMS}(T)$ is explained as follows. Suppose that the lattice constant $a_{IMS}$ of the triangular lattice in the vortex domains in the IMS is determined by the position $r_{min}$ of the potential minimum of the vortex-vortex interaction which is closely related to $\lambda$ [23,26,28]. In this case we can expect that during field-cooling vortices start to coalesce below a certain temperature $T_{IMS}$, where $r_{min}(T)$ becomes shorter than a vortex interval $a_B$ of the uniform Abrikosov lattice determined by the applied field. Hence, $a_{IMS}$ at $T_{IMS}$ is estimated to be $a_B$ using $a_B = (2\phi_0/\sqrt{3}B_{IMS})^{1/2}$, which is shown in the inset of Fig. 6. Here $\phi_0$ is the flux quantum, and $B_{IMS}$ is the magnetic induction just below $T_c$ [see Fig. 4(d)]. The temperature dependence of $a_{IMS}$ at the upper boundary of the IMS is fitted below 8 K by $a_{IMS}(T) \propto [1 - (T/T_c)^{(3-T/T_c)}]^{-1/2}$, which is derived from numerical solutions for the superconducting penetration depth in Bardeen-Cooper-Schrieffer theory and has been used as a fitting function for SANS data [26,28]. The obtained $a_{IMS}$ at 0 K is 176 nm, which is the almost same as a result of SANS [26], and approximately 4 times longer than reported $\lambda_{T=0}$ for pure Nb [22,46].

As discussed above, we expect the existence of the attractive interaction between vortices for cavity-grade Nb, which have an impact on the process of flux expulsion during cool down. For example, the degree of influence by various kinds of pinning centers, e.g., grain boundaries, impurities, precipitates, and so on, would be different in the two cases, i.e., isolated single vortices and the form of vortex bundles. Further observations of the clustering of vortices such as the vortex bundles in an actual environmental field for the SRF cavities (several tens of mGauss) and studies of their interaction with these pinning centers would be required to identify which pinning centers are more relevant to disturbance of the flux expulsion. MO imaging could provide a solution to study these problems.

## IV. SUMMARY

To confirm the existence of IMS in high-purity cavity-grade Nb crystals, we conducted *in situ* real-space observation

of the magnetic field distributions during the field-cooling and field-scanning processes in samples annealed at 900 °C using a magneto-optical imaging technique. In the field-cooling process we successfully observed evolution of phase separation into vortex and Meissner regions, as would be expected in the IMS. The size of the vortex regions, such as vortex bundles, in the IMS tends to be larger in higher fields. In the field-scanning process, domelike field profiles are observed, indicating a geometrical barrier with very weak bulk pinning. Our results are consistent with the view that the attractive interaction exists between vortices at the length scale of the penetration depth. This fact is likely to be important to explore ways to effectively expel the vortices in SRF cavities during cool down.

## ACKNOWLEDGMENTS

The authors would like to thank E. Kako, H. Sakai, and K. Tsuchiya for their close collaboration and advice. We also thank H. B. Wang and K. Hirata for the preparation of equipment in the early stages of this work. This study was supported by JSPS KAKENHI Grant No. 19H04402 and partially by JSPS KAKENHI Grant No. 19K05256.

## APPENDIX A: ESTIMATE $\kappa$ OF CAVITY-GRADE Nb

We can estimate the GL parameter $\kappa$ using the RRR value of Nb. From the microscopic derivation of the GL theory [47,48] it is known that

$$\kappa(\ell) = \frac{1}{\chi(a_{\rm imp})}\kappa_0, \tag{A1}$$

$$\chi(a_{\rm imp}) = \frac{8}{7\zeta(3)}\sum_{n=0}^{\infty}\frac{1}{(2n+1)^2[(2n+1)+a_{\rm imp}]}. \tag{A2}$$

Here $\kappa_0$ is the GL parameter of the pure material, $\chi$ is the so-called Gor'kov function, $a_{\rm imp} = (\pi/2e^{\gamma_E})(\xi_0/\ell) \simeq 0.882(\xi_0/\ell)$ is the Dirt parameter, $\gamma_E = 0.577$ is the Euler constant, and $\xi_0$ is the BCS coherence length. Now $\kappa$ is expressed with $\ell$; therefore, the next task is to express $\ell$ with RRR. According to Goodman and Kuhn [49], we have $\ell = (3.7\times10^{-16}\ \Omega\,{\rm m}^2)/\rho_n$. Using $\rho_n(295\ {\rm K}) \simeq 1.45\times10^{-7}\ \Omega\,{\rm m}$ [50] and $\rho_n \simeq {\rm RRR}^{-1}\times\rho_n(295\ {\rm K})$, we obtain

$$\ell = {\rm RRR}\times 2.55\ {\rm nm}. \tag{A3}$$

For our cavity-grade Nb with RRR = 500, we find $\ell = 1.3\ \mu{\rm m}$ ($a_{\rm imp} = 0.031 \ll 1$), which means the clean limit. Then Eq. (A1) yields $\kappa/\kappa_0 = 1.03$, which is close to the value of the ideal pure Nb.

## APPENDIX B: THEORY OF ASYMPTOTIC INTERACTION BETWEEN VORTICES

At $T \simeq T_c$, the well-known Abrikosov's solution of the GL equation offers a standard description of a vortex lattice. At lower temperatures, however, many features of the vortex lattice that cannot be described by the GL theory manifest themselves (e.g., vortex attraction). The microscopic theory is necessary to obtain a full picture of the vortex dynamics.

The theory of asymptotic interaction between vortices, the so-called asymptotic theory, provides a simple criterion for classifying superconductors into type II/1 (vortex-attraction regime) and type II/2 (vortex-repulsion regime) [44,51]. This theory evaluates the interaction between well-separated vortices based on the asymptotic solution of the Eilenberger equation for an isolated vortex [52]. The vortex interaction becomes attractive when (i) $\Lambda$ is real and $\Lambda < \xi$ or (ii) $\Lambda$ is complex. Here $\Lambda$ and $\xi$ are the decay length of the magnetic field and the order parameter, respectively. For the clean limit, $\Lambda$ and $\xi$ are determined by the following implicit equations:

$$1 = \frac{16}{\tilde{\kappa}^3}\frac{T}{T_c}\frac{\Lambda^3}{\xi_0^3}\left(\frac{k_BT_c}{\Delta_0}\right)^3\sum_m\frac{\Delta^2(T)u_1(z_m)}{(\hbar\omega_m)^2+\Delta^2(T)}, \tag{B1}$$

$$u_1(z_m) = \frac{z_m}{2} - \frac{z_m^2-1}{4}\ln\frac{z_m+1}{z_m-1}, \tag{B2}$$

$$z_m = \frac{2\Lambda}{\pi\xi_0}\frac{\sqrt{(\hbar\omega_m)^2+\Delta^2(T)}}{\Delta_0}, \tag{B3}$$

and

$$0 = \sum_m\left[\frac{\pi/2}{\sqrt{(\hbar\omega_m)^2+\Delta^2(T)}} - \frac{\xi}{\xi_0}\frac{\Delta^2(T)u_2(x_m)}{(\hbar\omega_m)^2+\Delta^2(T)}\right], \tag{B4}$$

$$u_2(x_m) = \frac{1}{2}\ln\frac{x_m+1}{x_m-1}, \tag{B5}$$

$$x_m = \frac{2\xi}{\pi\xi_0}\frac{\sqrt{(\hbar\omega_m)^2+\Delta^2(T)}}{\Delta_0}, \tag{B6}$$

respectively. Here $\Delta(T)$ is the BCS pair potential at $T$ in the zero-current state calculated from the BCS self-consistency equation, $\Delta_0 = \Delta(0)$ is the BCS pair potential at $T = 0$, $\xi_0$ is the BCS coherence length, $\hbar\omega_m = \pi k_BT(2m+1)$ is the Matsubara frequency, $\tilde{\kappa} = \sqrt{7\zeta(3)/18}\kappa$, and $\kappa$ is the GL parameter of the pure material. Equations (B1)–(B6) can be numerically solved for an arbitrary combination of $T$ and $\kappa$. By scanning the $T$-$\kappa$ plane and using these criteria, we obtain Fig. 6(b) in the main text.

It should be noted that the Eilenberger equation is numerically solved without approximation for a hexagonal vortex lattice [45], which offers a more quantitative description of the phase boundaries of type-II/1 and type-II/2 superconductors. The asymptotic theory is consistent with the full calculation at $t \gtrsim 0.5$ and is sufficient for qualitative discussions.

[1] M. H. Devoret and R. J. Schoelkopf, Science **339**, 1169 (2013).

[2] J. Zmuidzinas, Annu. Rev. Condens. Matter Phys. **3**, 169 (2012).

[3] H. Padamsee, Supercond. Sci. Technol. **30**, 053003 (2017).
[4] B. Aune, R. Bandelmann, D. Bloess, B. Bonin, A. Bosotti, M. Champion, C. Crawford, G. Deppe, B. Dwersteg, D. A. Edwards *et al.*, Phys. Rev. ST Accel. Beams **3**, 092001 (2000).
[5] H. Paik, D. I. Schuster, L. S. Bishop, G. Kirchmair, G. Catelani, A. P. Sears, B. R. Johnson, M. J. Reagor, L. Frunzio, L. I. Glazman *et al.*, Phys. Rev. Lett. **107**, 240501 (2011).
[6] M. Reagor, H. Paik, G. Catelani, L. Sun, C. Axline, E. Holland, I. M. Pop, N. A. Masluk, T. Brecht, L. Frunzio *et al.*, Appl. Phys. Lett. **102**, 192604 (2013).
[7] A. Grassellino, A. Romanenko, D. Sergatskov, O. Melnychuk, Y. Trenikhina, A. Crawford, A. Rowe, M. Wong, T. Khabiboulline, and F. Barkov, Supercond. Sci. Technol. **26**, 102001 (2013).
[8] P. Dhakal, G. Ciovati, G. R. Myneni, K. E. Gray, N. Groll, P. Maheshwari, D. M. McRae, R. Pike, T. Proslier, F. Stevie *et al.*, Phys. Rev. ST Accel. Beams **16**, 042001 (2013).
[9] A. Megrant, C. Neill, R. Barends, B. Chiaro, Y. Chen, L. Feigl, J. Kelly, E. Lucero, M. Mariantoni, P. J. J. O'Malley *et al.*, Appl. Phys. Lett. **100**, 113510 (2012).
[10] A. Nersisyan, S. Poletto, N. Alidoust, R. Manenti, R. Renzas, C.-V. Bui, K. Vu, T. Whyland, Y. Mohan, E. A. Sete *et al.*, in *Proceedings of the 2019 IEEE International Electron Devices Meeting (IEDM)* (IEEE, Piscataway, NJ, 2019), pp. 31.1.1–31.1.4.
[11] A. Gurevich, Phys. Rev. Lett. **113**, 087001 (2014).
[12] A. Gurevich and T. Kubo, Phys. Rev. B **96**, 184515 (2017).
[13] A. V. Semenov, I. A. Devyatov, P. J. de Visser, and T. M. Klapwijk, Phys. Rev. Lett. **117**, 047002 (2016).
[14] T. Kubo and A. Gurevich, Phys. Rev. B **100**, 064522 (2019).
[15] T. Kubo, Phys. Rev. Res. **2**, 013302 (2020).
[16] A. Gurevich and G. Ciovati, Phys. Rev. B **87**, 054502 (2013).
[17] D. B. Liarte, D. Hall, P. N. Koufalis, A. Miyazaki, A. Senanian, M. Liepe, and J. P. Sethna, Phys. Rev. Appl. **10**, 054057 (2018).
[18] M. Masuzawa, A. Terashima, K. Tsuchiya, and R. Ueki, Supercond. Sci. Technol. **30**, 034009 (2017).
[19] A. Romanenko, A. Grassellino, O. Melnychuk, and D. A. Sergatskov, J. Appl. Phys. **115**, 184903 (2014).
[20] S. Huang, T. Kubo, and R. L. Geng, Phys. Rev. Accel. Beams. **19**, 082001 (2016).
[21] S. Posen, M. Checchin, A. C. Crawford, A. Grassellino, M. Martinello, O. S. Melnychuk, A. Romanenko, D. A. Sergatskov, and Y. Trenikhina, J. Appl. Phys. **119**, 213903 (2016).
[22] D. K. Finnemore, T. F. Stromberg, and C. A. Swenson, Phys. Rev. **149**, 231 (1966).
[23] E. H. Brandt and M. P. Das, J. Supercond. Novel Magn. **24**, 57 (2011).
[24] H. Trauble and U. Essmann, Phys. Status Solidi **20**, 95 (1967).
[25] U. Essmann, Physica **55**, 83 (1971).
[26] A. Pautrat and A. Brûlet, J. Phys.: Condens. Matter **26**, 232201 (2014).
[27] T. Reimann, S. Mühlbauer, M. Schulz, B. Betz, A. Kaestner, V. Pipich, P. Böni, and C. Grünzweig, Nat. Commun. **6**, 8813 (2015).
[28] A. Backs, M. Schulz, V. Pipich, M. Kleinhans, P. Böni, and S. Mühlbauer, Phys. Rev. B **100**, 064503 (2019).
[29] J.-Y. Ge, J. Gutierrez, A. Lyashchenko, V. Filipov, J. Li, and V. V. Moshchalkov, Phys. Rev. B **90**, 184511 (2014).
[30] J.-Y. Ge, V. N. Gladilin, N. E. Sluchanko, A. Lyashenko, V. B. Filipov, J. O. Indekeu, and V. V. Moshchalkov, New J. Phys. **19**, 093020 (2017).
[31] I. Luk'yanchuk, Phys. Rev. B **63**, 174504 (2001).
[32] A. Vagov, S. Wolf, M. D. Croitoru, and A. A. Shanenko, Commun. Phys. **3**, 58 (2020).
[33] A. A. Polyanskii, P. J. Lee, A. Gurevich, Z.-H. Sung, and D. C. Larbalestier, in *Symposium on the Superconducting Science and Technology of Ingot Niobium* (AIP, New York, 2011).
[34] J. Köszegi, O. Kugeler, D. Abou-Ras, J. Knobloch, and R. Schäfer, J. Appl. Phys. **122**, 173901 (2017).
[35] H. W. Weber, M. Botlo, F. M. Sauerzopf, H. Wiesinger, and U. Klein, Jpn. J. Appl. Phys. **26**, 917 (1987).
[36] A. Ikushima and T. Mizusaki, J. Phys. Chem. Solids **30**, 873 (1969).
[37] See Supplemental Material at http://link.aps.org/supplemental/10.1103/PhysRevB.104.064504 for two movies corresponding to Figs. 4 and 5, an example of conversion procedure, and difference of vortex-bundle patterns in different cooling cycles.
[38] A. Moreno and H. Ferrari, Phys. B: Condens. Matter **407**, 3117 (2012).
[39] R. Prozorov, Phys. Rev. Lett. **98**, 257001 (2007).
[40] R. Prozorov, A. F. Fidler, J. R. Hoberg, and P. C. Canfield, Nat. Phys. **4**, 327 (2008).
[41] E. Zeldov, A. I. Larkin, V. B. Geshkenbein, M. Konczykowski, D. Majer, B. Khaykovich, V. M. Vinokur, and H. Shtrikman, Phys. Rev. Lett. **73**, 1428 (1994).
[42] E. Zeldov, A. Larkin, M. Konczykowski, B. Khaykovich, D. Majer, V. Geshkenbein, and V. Vinokur, Physica C **235–240**, 2761 (1994).
[43] G. Blatter and V. B. Geshkenbein, *Superconductivity* (Springer, Berlin, 2008).
[44] L. Kramer, Z. Phys. A: Hadrons Nucl. **258**, 367 (1973).
[45] U. Klein, J. Low Temp. Phys. **69**, 1 (1987).
[46] B. W. Maxfield and W. L. McLean, Phys. Rev. **139**, A1515 (1965).
[47] L. P. Gor'kov, Sov. Phys. JETP **9**, 1364 (1959).
[48] L. P. Gor'kov, Sov. Phys. JETP **10**, 998 (1960).
[49] B. B. Goodman and G. Kuhn, J. Phys. (Paris) **29**, 240 (1968).
[50] C. Kittel, *Introduction to Solid State Physics*, 8th ed. (John Wiley & Sons, New York, 2004).
[51] M. C. Leung, J. Low Temp. Phys. **12**, 215 (1973).
[52] G. Eilenberger and H. Büttner, Z. Phys. **224**, 335 (1969).